Coastal Engineering 210 (2026) 105055

Contents lists available at ScienceDirect

Coastal Engineering

journal homepage: www.elsevier.com/locate/coastaleng

Wave-induced overturning moments, moment arms, and associated forces on monopile foundations

Thobani Hlophe [a,b,*], Thomas A.A. Adcock [a], Haoyu Ding [c,d], Jun Zang [c], Paul H. Taylor [b]

[a] Department of Engineering Science, University of Oxford, Oxford, OX1 3PJ, UK
[b] School of Earth and Oceans, University of Western Australia, Perth, Western Australia, 6009, Australia
[c] Department of Architecture and Civil Engineering, University of Bath, Bath, BA2 7AY, UK
[d] Dalian State Key Laboratory of Offshore Renewable Energy, Dalian University of Technology, Dalian, 116024, China

ARTICLE INFO

Keywords:
Wave-induced moments
Monopile foundations
Offshore wind
Higher-order harmonics
CFD validation

ABSTRACT

Accurate prediction of wave-induced overturning moments is important for the safe and economical design of monopile foundations for offshore wind turbines. In this study, harmonic-specific moment arms are derived from depth integrals of the inertia force contribution up to the still-water level, yielding closed-form expressions for the effective moment arm associated with each force harmonic. These expressions are assessed against OpenFOAM simulations in an inertia-dominated regime. The results show that the inertia-based formulation, combined with modest harmonic-dependent corrections, reproduces the total overturning moment with high accuracy. Although the present validation uses simulated force harmonics, the same framework can be combined directly with higher-order Stokes-type force models for engineering applications.

1. Introduction

Bottom-mounted vertical cylinders, such as monopiles supporting offshore wind turbines, experience complex wave-induced loads comprising both horizontal forces and overturning moments about the seabed. While hydrodynamic forces on these structures have been studied extensively, the corresponding overturning moments have received comparatively less direct attention in either laboratory or numerical investigations. This gap is noteworthy because the mudline overturning moment is a primary driver for foundation sizing and structural integrity (Ryan et al., 2025).

The overturning moment may be related to the horizontal force through an effective moment arm, defined as the distance from the seabed to the effective point of action of the horizontal load. As with the force, the moment response is more nonlinear than the local wave field. High-quality wave flume measurements in the inertia regime by Feng et al. (2020) showed that higher bound harmonics of the overturning moment can exceed, in relative amplitude, the corresponding harmonics of the horizontal force. This reflects the increasing length of moment arms associated with higher force harmonics (i.e. the load at higher bound harmonics acts closer to the free surface). Using irregular waves, Horn et al. (2016) further demonstrated that higher-order forces become even more important when structural damping is low and that higher-order moment terms can dominate fatigue damage in energetic sea states. Empirical calculations by Feng et al. (2020) further showed that nondimensional moment arms remain approximately constant with increasing wave steepness for most harmonics, with the third harmonic as a notable exception. That harmonic tends to act close to the still-water level, consistent with the point-load assumptions in widely used nonlinear force models (Manners and Rainey, 1992; Faltinsen et al., 1995). The same behaviour is observed in the numerical results presented here.

Because overturning moments have received less dedicated study, the present work builds on the depth-distributed part of the nonlinear force model of Faltinsen, Newman and Vinje (FNV; Faltinsen et al., 1995) to derive harmonic-specific estimates for the effective moment arms. These expressions are obtained by integrating the depth-dependent acceleration terms of the FNV formulation and allow direct calculation of overturning moments once the horizontal force is known. The theory is tested using incompressible Navier–Stokes simulations of wave-induced forces and moments on a fixed vertical cylinder performed with `OpenFOAM`. By quantifying the effective moment arm and isolating higher-order contributions, the analysis clarifies the physical mechanisms controlling overturning moments. It provides a practical framework for engineering design of monopile-type foundations.

In practice, the nonlinear horizontal force may be modelled using well-validated Stokes-type models developed over the past decade (e.g. Chen et al., 2018; Tang et al., 2024b; Hlophe et al., 2025a,b), which are fitted to data-derived harmonic force coefficients and accurately

* Corresponding author at: Department of Engineering Science, University of Oxford, Oxford, OX1 3PJ, UK.
E-mail address: thobani.hlophe@uwa.edu.au (T. Hlophe).

https://doi.org/10.1016/j.coastaleng.2026.105055
Received 14 November 2025; Received in revised form 7 May 2026; Accepted 12 May 2026
Available online 18 May 2026

predict higher-order harmonics based solely on the linear Morison force time series. Coupling these Stokes-based force predictions with the present FNV-derived moment arms enables accurate prediction of the full overturning moment time history.

The remainder of the paper is organised as follows. Moment arms derived from the FNV model are presented in Section 2. The CFD simulations performed using OpenFOAM for a range of cylinder diameters and wave conditions are described in Section 3. Analysis of the CFD data, including comparisons between reconstructed and simulated moment histories, is provided in Section 4. The main conclusions are summarised in Section 5.

2. Theoretical derivation of moment arms

A right-handed Cartesian coordinate system is adopted, with the x-axis horizontal and aligned with the incident wave propagation direction, and the z-axis positive upwards, with its origin at the still-water level. The undisturbed flow is assumed two-dimensional, such that no y-components are present. The seabed is located at $z = -h$, where h denotes the still-water depth, and the instantaneous free surface is given by $z = \eta(x,t)$, where t is time. All overturning moments are taken about the mudline point $(x,z) = (0,-h)$.

Throughout this paper, subscripts (x,z,t) denote partial derivatives, e.g. $u_t \equiv \partial u/\partial t$, while indices (n,i,j) denote harmonic numbers, e.g. u_n is the nth harmonic component of the velocity u.

2.1. FNV formulation for forces and moments

The FNV formulation (Kristiansen and Faltinsen, 2017) provides a compact description of nonlinear wave loading on slender vertical cylinders by expressing the hydrodynamic force directly in terms of the undisturbed incident wave kinematics. Unlike diffraction-based approaches, which require solving a boundary-value problem on the body surface, the FNV model assumes that the cylinder diameter is small relative to the wavelength, such that wave scattering can be neglected. When this slender-body assumption is satisfied, force contributions up to third order in wave amplitude can be retained to estimate nonlinear wave loads.

Within this framework, the total horizontal force is expressed as the sum of a depth-distributed pressure loading and a localised free-surface contribution. The present section focuses on the distributed contribution, which forms the basis for the analytical moment-arm kernels derived below.

The distributed horizontal force per unit length follows the formulations of Manners and Rainey (1992) and Kristiansen and Faltinsen (2017), derived from the unsteady Bernoulli equation evaluated on the cylinder axis. This yields three distinct contributions:

$$\mathrm{d}F(z,t) = \rho\pi R^2 \left(C_m \frac{\partial u}{\partial t} + u\frac{\partial u}{\partial x} + C_m w \frac{\partial u}{\partial z} \right) \mathrm{d}z, \qquad -h \le z \le \eta(t), \tag{2.1}$$

where $u = \partial\Phi/\partial x$ and $w = \partial\Phi/\partial z$ are the horizontal and vertical velocity components of the incident flow, Φ is the velocity potential, and R is the monopile radius. The coefficient $C_m = 1 + C_a$ in the first and third terms incorporates the added-mass coefficient C_a associated with surge motion (Kristiansen and Faltinsen, 2017). In the present work, C_a is set to 1, corresponding to the potential flow value.

The first term in (2.1) corresponds to the inertia force proportional to the local fluid acceleration, while the second and third terms represent convective accelerations in the horizontal and vertical directions, respectively. Together, these form a nonlinear extension of the classical Morison inertia term.

In addition to the distributed load, the FNV formulation introduces a higher-order 'point-load' correction located at the free surface, originating from cubic interactions in the velocity potential. This contribution has the form

$$F_{\mathrm{PL}}(t) = \rho\pi R^2 \frac{4}{g} u^2 \frac{\partial u}{\partial t}, \tag{2.2}$$

evaluated at the cylinder axis $(x,z) = (0,0)$. Although often small compared with the distributed terms, this component becomes relevant in steep wave conditions where nonlinear free-surface effects are significant. The total horizontal force is therefore written as

$$F_{\mathrm{FNV}}(t) = \int_{z=-h}^{\eta(t)} \mathrm{d}F(z,t) + F_{\mathrm{PL}}(t), \tag{2.3}$$

and the overturning moment about the seabed is obtained by

$$M_{\mathrm{FNV}}(t) = \int_{-h}^{\eta(t)} (z+h)\,\mathrm{d}F(z,t) + (h+\eta(t))\,F_{\mathrm{PL}}(t), \tag{2.4}$$

where $(z+h)$ is the moment arm about the mudline $z = -h$. The free-surface point-load contribution is not included in the moment-arm kernels derived below, because it represents a surface-localised force whose effective moment arm lies close to the free surface. Its influence is instead reflected in the data-derived moment arms discussed in Section 4.2.1.

This framework links the harmonic expansion of the incident wave potential directly to the resulting hydrodynamic force and overturning-moment time series. The inertia term, proportional to the fully nonlinear fluid acceleration $\partial u/\partial t$, provides the dominant contribution to responses from linear to nonlinear, while the convective terms ($u\frac{\partial u}{\partial x}$ and $w\frac{\partial u}{\partial z}$), being quadratic, introduce additional higher-order contributions arising from the fully nonlinear kinematics. These nonlinear terms grow with wave amplitude and harmonic number, enabling the FNV formulation to capture the amplification of forces (and overturning moments) in steep and nonlinear wave fields, where linearised approaches are inadequate.

2.2. Depth functions and super-harmonic moment arms

The velocity field associated with nonlinear waves is written in a separable form in the vertical and horizontal coordinates. In a Stokes-type expansion, the horizontal and vertical velocity components may be expressed as

$$\begin{aligned} u(x,z,t) &= \sum_{n=1}^{N} \omega\, a(ka)^{n-1}\, C_n^x(k,\omega)\, \Psi_n^x(z)\, \Theta_n^x(x,t), \\ w(x,z,t) &= \sum_{n=1}^{N} \omega\, a(ka)^{n-1}\, C_n^z(k,\omega)\, \Psi_n^z(z)\, \Theta_n^z(x,t), \end{aligned} \tag{2.5}$$

where ω is the angular frequency, k is the wavenumber, a is the linear wave amplitude and ka is the wave steepness.

The prefactor $a(ka)^{n-1}$ captures the amplitude scaling of the nth bound harmonic in a Stokes expansion, while the coefficients C_n^x and C_n^z are dimensionless shape coefficients that depend on (k,ω) (and implicitly on water depth through kh), but not on the wave amplitude. The vertical structure is carried exclusively by the depth functions $\Psi_n^x(z)$ and $\Psi_n^z(z)$ defined in (2.6), and the temporal and spatial phase is described by

$$\Theta_n^x = \cos\left[n(kx - \omega t + \epsilon_0)\right], \qquad \Theta_n^z = \sin\left[n(kx - \omega t + \epsilon_0)\right],$$

where ϵ_0 is the initial phase shift.

This representation is consistent with linear wave theory for $n = 1$ and extends naturally to higher bound harmonics through the Stokes-type scaling, allowing the vertical dependence of each harmonic contribution to be treated independently of its amplitude.

The present representation includes only oscillatory (non-zero-frequency) harmonics with $n \ge 1$; the close-to-zero-frequency ($n = 0$) contribution, which is predominantly second order in wave amplitude and associated with mean and slowly varying loads, is discussed separately in Section 2.3 as a limit.

For each harmonic number n, the vertical structure functions are

$$\Psi_n^x(z) = \frac{\cosh[nk(z+h)]}{\sinh nkh}, \qquad \Psi_n^z(z) = \frac{\sinh[nk(z+h)]}{\sinh nkh}. \tag{2.6}$$

These functions satisfy the Laplace equation and continuity condition for potential flow theory.

Similarly, the free-surface elevation may be expressed as a sum of harmonics of the form

$$\eta(t) = \sum_{n=1}^{N} \eta_n(t), \qquad \eta_n \propto a(ak)^{n-1} \cos\left[n(kx - \omega t + \epsilon_0)\right]. \tag{2.7}$$

The harmonics for force and moment follow directly from the wave kinematics. This harmonic-by-harmonic formalism is essential for quantifying the nonlinear amplification of overturning moments arising from higher-order wave terms.

Throughout this study, we evaluate the depth integrals with the upper limit fixed at the still-water level $z = 0$. This choice does not imply linear kinematics: higher bound harmonics are retained in u and w. Rather, fixing the integration limit provides an amplitude-independent baseline kernel for the moment arm. If the upper limit is taken as $z = \eta(t)$, then an expansion

$$\int_{-h}^{\eta(t)} (\cdot)\,\mathrm{d}z = \int_{-h}^{0} (\cdot)\,\mathrm{d}z + \eta(t)\,(\cdot)\Big|_{z=0} + \tfrac{1}{2}\eta(t)^2\,\partial_z(\cdot)\Big|_{z=0} + \cdots$$

shows that additional contributions arise at the same harmonic order through products. These terms act near the free surface and therefore shift the effective moment arm upwards. In Section 4 we account for the leading impact of these contributions via harmonic-dependent corrections, and Appendix provides an explicit illustration for the second harmonic.

The effective moment arm for the nth harmonic is therefore defined as the ratio of the corresponding overturning moment to the horizontal force:

$$L_n = \frac{M_n}{F_n} = \frac{\displaystyle\int_{-h}^{0} (z+h)\,\mathrm{d}F_n(z,t)}{\displaystyle\int_{-h}^{0} \mathrm{d}F_n(z,t)}. \tag{2.8}$$

The expressions below are derived from Eq. (2.8) under the following assumptions:

(a) A uniform, vertical circular cylinder in finite depth is considered, with force contributions obtained by depth-integration of linear vertical eigenfunctions.
(b) The velocity potential is expanded into harmonics consistent with a Stokes-type series.
(c) Slender-body assumptions are implicit, neglecting diffraction and higher-order cross terms in the cylinder's horizontal extent.

These expressions provide explicit formulae for the effective lever arms of both inertia and convective terms within the FNV formalism. They illustrate how higher-order nonlinearities redistribute the depth profile of the loading, shifting the centre of action of forces and amplifying the overturning moment.

2.2.1. Inertia term (u_t)

For the inertia-related contribution, the force per unit length associated with the nth harmonic can be written as

$$F_n^{(u_t)}(z,t) \;\propto\; n\omega^2\,(ka)^{n-1}\,C_n^x(k,\omega)\,\Psi_n^x(z)\,\tfrac{\mathrm{d}}{\mathrm{d}t}\Theta_n^x. \tag{2.9}$$

Since all prefactors are independent of z, they cancel identically between the numerator and denominator of Eq. (2.8). Consequently, the moment arm depends only on the vertical structure function $\Psi_n^x(z)$. In other words, the ratio (2.8) is determined entirely by the depth dependence (numerator) of $\Psi_n^x(z)$.

Carrying out the integration yields a closed-form expression:

$$L_n^{(u_t)} = \frac{\Lambda_n - \coth\Lambda_n + \operatorname{csch}\Lambda_n}{n\hat{k}}, \qquad \Lambda_n \equiv n\,\hat{k}\,h, \tag{2.10}$$

where $\hat{k}$ denotes the effective wavenumber associated with the wave field. Here $\hat{k}$ is the linear wavenumber associated with an equivalent wave period used to evaluate the moment-arm kernels. In the present work, $\hat{k}$ is obtained from the linear dispersion relation $\omega^2 = g\hat{k}\tanh(\hat{k}h)$, with $\omega = 2\pi/T_{m02}$, where g is the gravitational acceleration and T_{m02} is the zero-crossing period of the extracted first-harmonic free-surface elevation. The practical evaluation of T_{m02} is described in Section 4.2.

2.2.2. Convective acceleration terms (uu_x and wu_z)

The convective acceleration terms arise from quadratic products of the velocity field components, generating nonlinear harmonic interactions. For clarity, we distinguish between the harmonic indices i and j associated with the two factors in the product.

The two relevant quadratic terms are

$$u_i \frac{\partial u_j}{\partial x} \;\propto\; jk\cosh[ik(h+z)]\,\cosh[jk(h+z)], \tag{2.11}$$

$$w_i \frac{\partial u_j}{\partial z} \;\propto\; jk\sinh[ik(h+z)]\,\sinh[jk(h+z)]. \tag{2.12}$$

Following the definition of the effective moment arm (2.8), depth integration leads to closed-form expressions that depend only on the nondimensional combinations

$$\Lambda_{i\pm j} \;\equiv\; (i \pm j)\,\hat{k}\,h.$$

For the uu_x contribution, the effective moment arm becomes

$$L_{i,j}^{(uu_x)} = h + \frac{(i+j)^2 + (i-j)^2 - (i+j)^2\cosh\Lambda_{i-j} - (i-j)^2\cosh\Lambda_{i+j}}{\hat{k}\,(i-j)(i+j)\,\left[(i+j)\sinh\Lambda_{i-j} + (i-j)\sinh\Lambda_{i+j}\right]}, \tag{2.13}$$

while the wu_z contribution takes the form

$$L_{i,j}^{(wu_z)} = h + \frac{(i+j)^2 - (i-j)^2 - (i+j)^2\cosh\Lambda_{i-j} + (i-j)^2\cosh\Lambda_{i+j}}{\hat{k}\,(i-j)(i+j)\,\left[(i+j)\sinh\Lambda_{i-j} - (i-j)\sinh\Lambda_{i+j}\right]}. \tag{2.14}$$

The quadratic terms (uu_x and wu_z) generate contributions at both the sum and difference harmonics, $n = i + j$ and $n = |i - j|$, which enter through the combinations $\Lambda_{i\pm j}$ in the expressions above. Thus, the effective moment arms depend on both the sum and difference interactions of the contributing harmonics. Both expressions are well defined for $i \neq j$, but for self-interactions ($i = j$), the denominators vanish, yielding indeterminate $\frac{0}{0}$ forms. Physically, this corresponds to the situation where a single harmonic interacts with itself, and the limiting behaviour must be evaluated carefully. Taking the limit $j \to i$ gives the self-interaction results.

For the uu_x term,

$$L_{i,i}^{(uu_x)} = \frac{\Lambda_i^2 - \sinh^2\Lambda_i + \Lambda_i\,\sinh 2\Lambda_i}{i\,\hat{k}\,\left(2\Lambda_i + \sinh 2\Lambda_i\right)}, \tag{2.15}$$

and for the wu_z term,

$$L_{i,i}^{(wu_z)} = \frac{\Lambda_i^2 + \sinh^2\Lambda_i - \Lambda_i\,\sinh 2\Lambda_i}{i\,\hat{k}\,\left(2\Lambda_i - \sinh 2\Lambda_i\right)}, \tag{2.16}$$

where

$$\Lambda_i \;\equiv\; i\,\hat{k}\,h.$$

These expressions show that the convective moment arms depend nonlinearly on harmonic order and remain sensitive to finite depth through the hyperbolic terms.

These convective arm expressions are included for completeness; in the inertia-dominated cases analysed here, their net contribution to the integrated force and moment is small, and the reconstructions below therefore use inertia-based arms.

2.3. The zeroth-harmonic and long-wave limits

The slowly varying (mean or set-down) component of the load can be interpreted in two equivalent ways, assuming a finite depth h: (i) the *zeroth-harmonic limit*, obtained by letting the harmonic number $n \to 0$ in the series expansion, and (ii) the *long-wave (shallow-water) limit*, obtained when the nondimensional water depth $\hat{k}h \to 0$. Physically, these limits coincide because both correspond to slowly varying loading with a vertical structure that is nearly uniform over the water column. The relevant small parameter is then the product $\Lambda_n \equiv n\hat{k}h$. Hence, the asymptotics are governed by the single condition $\Lambda_n \to 0$, which may be achieved by small n, small $\hat{k}h$, or both.

2.3.1. Inertia term (u_t)

For the inertia contribution, performing a Taylor expansion of Eq. (2.10) in Λ_n gives

$$L_n^{(u_t)} = \frac{h}{2} + \frac{\Lambda_n^2 h}{24} - \frac{\Lambda_n^4 h}{240} + O(\Lambda_n^6).$$

Taking the exact limit $\Lambda_n \to 0$ yields

$$\lim_{\Lambda_n \to 0} L_n^{(u_t)} = \frac{h}{2}, \tag{2.17}$$

which is effectively the centroid of the water column.

2.3.2. Convective acceleration terms (uu_x and wu_z)

For the uu_x self-interaction, the moment arm is Eq. (2.15), with $i \to n$. The small-Λ_n expansion yields

$$L_n^{(uu_x)} = \frac{h}{2} + \frac{\Lambda_n^2 h}{12} - \frac{\Lambda_n^4 h}{180} + O(\Lambda_n^6).$$

Therefore, the zero limit is

$$\lim_{\Lambda_n \to 0} L_n^{(uu_x)} = \frac{h}{2}. \tag{2.18}$$

Thus, the uu_x convective term has the same centroidal mean location as the inertia term u_t. Similarly, the expansion for wu_z (2.16) gives

$$L_n^{(wu_z)} = \frac{3}{4}h + \frac{\Lambda_n^2 h}{60} - \frac{\Lambda_n^4 h}{1050} + O(\Lambda_n^6),$$

with a limit

$$\lim_{\Lambda_n \to 0} L_n^{(wu_z)} = \frac{3}{4}h. \tag{2.19}$$

Unlike the u_t and uu_x terms, the wu_z contribution has its effective centroid located at three-quarters of the total depth. All three terms, therefore, admit well-defined zero limits. This distinction is important when considering the mean (set-down) load distribution.

Figs. 1–2 summarise the depth-dependent moment-arm kernels for the various quadratic terms. A progressive increase in the lever arms is observed in both the inertia u_t curves and the convective terms. As expected, the convective contributions exhibit a symmetry property: identical results are obtained for cases with constant $|i - j|$ as well as for constant $i + j$. The lever arms grow systematically with increasing $i + j$.

Interestingly, the contribution of the convective interaction $u_i \partial u_j / \partial x$ approaches that of the inertia term $\partial u_n / \partial t$ when the harmonic number follows the sum interaction $n = i + j$ (Fig. 3 panel (a)). Furthermore, the convective self-interaction cases ($j \to i = n$, for uu_x and wu_z) are consistent with the corresponding off-diagonal interactions ($i \neq j$), provided that the effective harmonic indices satisfy $2n = i + j$ (Fig. 3 panels (b, c)). This agreement holds for all values of kh, and becomes increasingly robust as $|i - j| \to 0$, reinforcing the interpretation that quadratic interactions are governed primarily by the effective harmonic number rather than the specific pair of interacting modes.

3. Numerical simulations (CFD)

This section describes the numerical wave tank setup, wave generation, and post-processing used in the CFD simulations.

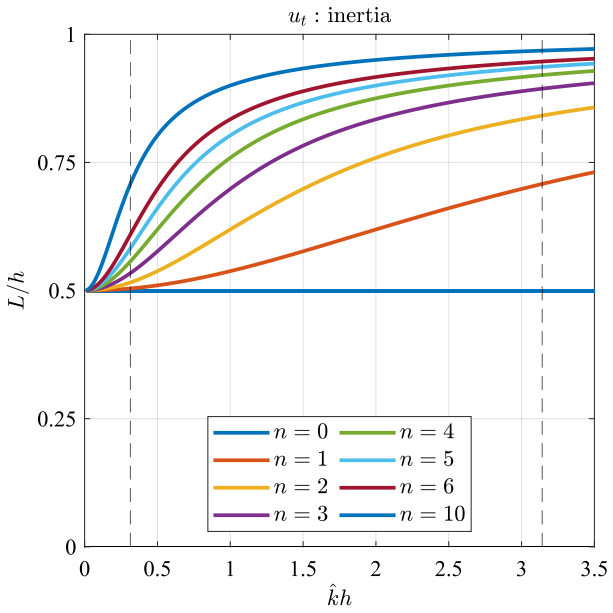

Fig. 1. Dimensionless moment-arm kernels for the inertia term u_t, plotted for harmonic indices $n \in [0, 10]$. The vertical dashed grey lines mark the boundaries of the intermediate-depth regime.

3.1. Numerical model and scope

All simulations were performed using OpenFOAM with a two-phase (air–water) incompressible volume-of-fluid (VOF) solver for the Navier–Stokes equations. Turbulence was modelled using the k–ω SST RANS closure. For the present wave and cylinder parameters, the integrated viscous contribution to the horizontal force and mudline overturning moment was found to be small compared with the pressure contribution (typically $\lesssim$ a few per cent), consistent with an inertia-dominated loading regime.

3.2. Wave type and phase-based simulations

All simulations use NewWave-type (Tromans et al., 1991) focused wave groups prescribed through *waves2Foam* (Jacobsen et al., 2012). For each case, four runs were performed with identical linear amplitude spectra but different global phase shifts $\epsilon_0 \in \{0°, 90°, 180°, 270°\}$. This enables harmonic separation following the phase-manipulation approach of Fitzgerald et al. (2014). The characteristic period reported in Table 1 is the target peak period T_p of the underlying spectrum, and the focal point is located at the cylinder centre.

For clarity throughout the remainder of this paper, we stress that phase manipulation (and similar) refers explicitly to the change of the phase of the input wave group (the position of the wiggles within the wave envelope), not to the two phases (air and water) assumed present in the fluid domain for any individual CFD simulation.

3.3. Computational domain and boundary conditions

A vertical cylinder of radius $0.1 \leq R \leq 0.2$ m was positioned at the centre of a numerical wave tank. Relaxation zones were applied at both inlet and outlet boundaries to generate and absorb waves, each extending 1.5 times the peak incident wavelength. This allowed the total domain length to be reduced to approximately seven peak wavelengths without introducing significant reflection effects, following Jacobsen et al. (2012).

Boundary conditions were prescribed as follows: the seabed and cylinder surfaces used no-slip wall boundary conditions; the top boundary was treated as atmosphere; inlet and outlet boundaries employed

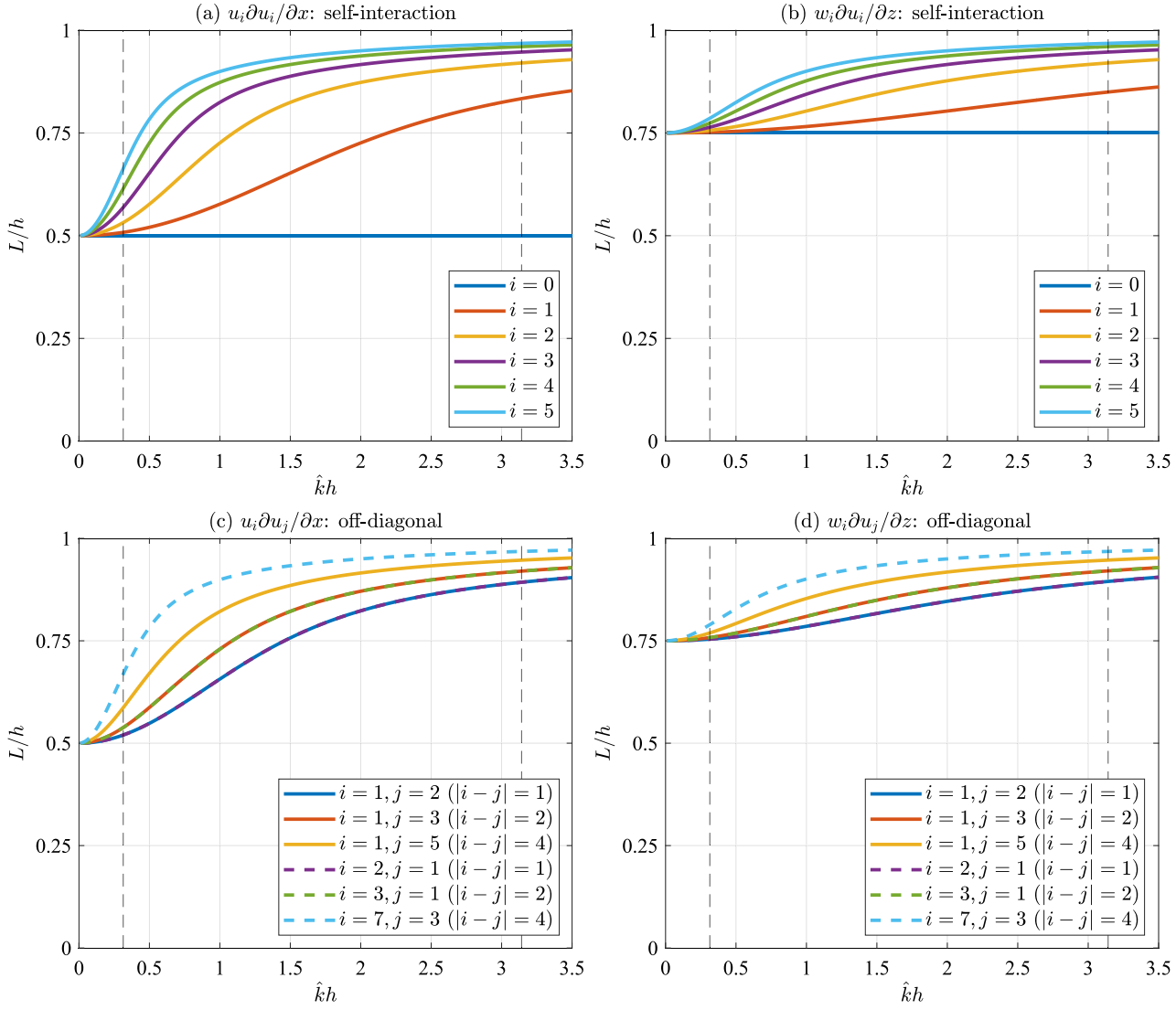

Fig. 2. Dimensionless moment-arm kernels for convective terms. (a) $u_i\partial u_i/\partial x$ self-interaction ($i = j$); (b) $w_i\partial u_i/\partial z$ self-interaction ($i = j$); (c) $u_i\partial u_j/\partial x$ off-diagonal ($i \neq j$) grouped by $|i - j|$; (d) $w_i\partial u_j/\partial z$ off-diagonal. The vertical dashed grey lines mark the boundaries of the intermediate-depth regime.

Table 1
Parameters of the CFD simulations. a is the linear wave amplitude (recalculated from η time histories), η_{max} the prescribed maximum wave crest elevation, T_p the prescribed peak wave period, k_ph the nondimensional depth, k_pa the (linear) wave steepness, $k_p\eta_{max}$ the (nonlinear) wave steepness, k_pR the relative cylinder diameter, $KC = \pi\eta_{max}/R$ the Keulegan–Carpenter number, and $Fr = 2\pi\eta_{max}/(T_p\sqrt{2gR})$ the Froude number.

Case	a (m)	η_{max} (m)	T_p (s)	k_ph	k_pa	$k_p\eta_{max}$	k_pR	KC	Fr
CFD-01	0.208	0.240	2.52	1.32	0.152	0.176	0.147	3.77	0.302
CFD-02	0.272	0.380	2.52	1.32	0.199	0.278	0.147	5.97	0.479
CFD-03	0.246	0.300	2.52	1.32	0.180	0.220	0.147	4.71	0.378
CFD-04	0.275	0.340	2.52	1.32	0.202	0.249	0.147	5.34	0.428
CFD-05	0.321	0.440	3.30	0.92	0.164	0.224	0.102	6.91	0.423
CFD-06	0.256	0.300	3.30	0.92	0.131	0.153	0.102	4.71	0.288
CFD-07	0.337	0.500	3.30	0.92	0.172	0.255	0.102	7.85	0.481
CFD-08	0.207	0.240	2.53	1.31	0.151	0.175	0.0728	7.54	0.426
CFD-09	0.207	0.240	2.53	1.31	0.151	0.175	0.109	5.03	0.347
CFD-10	0.207	0.240	2.53	1.31	0.151	0.175	0.146	3.77	0.301
CFD-11	0.278	0.380	2.53	1.31	0.202	0.276	0.0728	11.90	0.674
CFD-12	0.278	0.380	2.53	1.31	0.202	0.276	0.109	7.96	0.550
CFD-13	0.278	0.380	2.53	1.31	0.202	0.276	0.146	5.97	0.476
CFD-14	0.324	0.500	2.53	1.31	0.235	0.364	0.0728	15.70	0.887
CFD-15	0.324	0.500	2.53	1.31	0.235	0.364	0.109	10.50	0.724
CFD-16	0.324	0.500	2.53	1.31	0.235	0.364	0.146	7.85	0.627

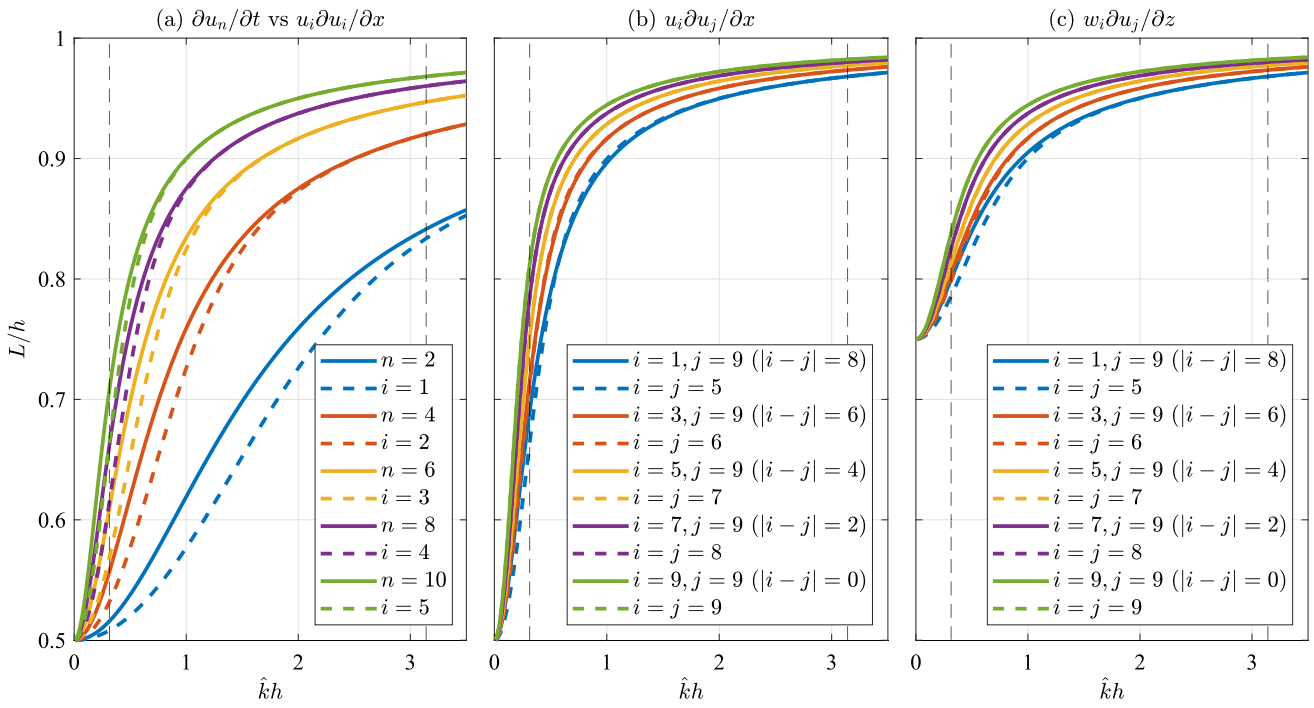

Fig. 3. Comparison between inertia and convective moment-arm kernels. (a) Inertia term $\partial u_n/\partial t$ versus the self-interaction convective $u_i \partial u_i/\partial x$ with $n = i + i$, showing near-equivalence across all depths as n increases. (b) Convective term $u_i \partial u_j/\partial x$ off-diagonal ($i \neq j$) compared against the self-interaction at $(i + j)/2$, illustrating collapse of the kernels for matching harmonic sums. (c) Analogous comparison for $w_i \partial u_j/\partial z$, likewise showing convergence between off-diagonal and self-interaction when $|i - j| \to 0$. The vertical dashed grey lines mark the boundaries of the intermediate-depth regime.

relaxation zones for wave generation and absorption; and the lateral boundary was treated as a symmetry plane in half-domain simulations. A half-domain formulation was used for the present head-on focused-wave, vertical-cylinder configuration, which is symmetric about the longitudinal centre plane. The lateral boundary was therefore treated as a symmetry plane following Chen et al. (2014). Exploiting this symmetry allowed only half of the wave tank to be simulated, thereby reducing computational cost. This assumption is appropriate for the present configuration, where both the incident wave field and the structural geometry are symmetric about the centre plane.

3.4. Mesh resolution and time stepping

The computational mesh followed the resolution recommendations of Chen et al. (2014), with horizontal spacing $\Delta x = \Delta y = \lambda_p/240$ and vertical spacing $\Delta z = a/8$, where λ_p and a denote the peak incident wavelength and linear wave amplitude, respectively. To improve resolution in the vicinity of the cylinder, the innermost mesh layers were refined to 0.2 times the thickness of the coarsest vertical layer, following Ding et al. (2025).

Time advancement employed adaptive time stepping with a maximum Courant number of 0.5. Maintaining a small Courant number is essential for accurately resolving subsurface velocity kinematics in VOF-based wave simulations and for reliable force prediction (see, e.g. Larsen et al., 2019; Li and Fuhrman, 2022).

3.5. Force and moment extraction

Hydrodynamic forces and overturning moments acting on the cylinder were obtained using the standard `forces` function object in OpenFOAM, which integrates pressure and viscous stresses over the wetted surface. The overturning moment was evaluated about the cylinder base using the same stress distribution.

To enable harmonic-by-harmonic analysis, time histories of the free-surface elevation η, horizontal force F, and overturning moment M were recorded for each of the four phase-shifted simulations. Simulation parameters for all cases are summarised in Table 1. In all simulations, the prescribed wave parameters were the maximum crest elevation $\eta_{\max}$ and the peak period T_p, with the linear wave amplitude a recalculated from the η time histories simulated without the cylinder in the numerical tank, commonly referred to as 'empty-tank' simulations.

Cylinder radius $R = 0.20$ m was used for cases CFD-01 to CFD-07, followed by three repeats with $R = 0.10$, 0.15, and 0.20 m for cases CFD-08 to CFD-16. The tabulated dimensionless parameters include the Keulegan–Carpenter number and Froude number, defined as

$$KC = \pi \eta_{\max}/R, \qquad Fr = \frac{2\pi \eta_{\max}}{T_p \sqrt{2gR}},$$

which characterise the flow regime. For reference, the secondary load cycle becomes noticeable at approximately $KC \approx 5.5$ and $Fr \approx 0.44$, and becomes distinct at $KC \approx 6.4$ and $Fr \approx 0.51$, consistent with Hlophe et al. (2025b).

3.6. Validation and qualitative wave–structure interaction

Following the same numerical wave tank setup as in previous related work (Ding et al., 2025), validation tests showed good agreement between OpenFOAM and experiments for fully nonlinear wave–cylinder interactions.

Fig. 4 illustrates the CFD-02 case. The free-surface elevation shows the incident focused wave at the cylinder location, while the corresponding force time history exhibits characteristic oscillations immediately following the main crest. Examination of the wave field at the three marked time instants ***a***, ***b***, and ***c*** reveals strong wave scattering around the cylinder. As also discussed by Ding et al. (2025), a thin fluid sheet wraps around the upstream face of the cylinder at ***a***, followed by fluid accumulation at the rear at ***b***. These processes contribute to the oscillatory features in the force signal, while the backward run-up observed at ***c*** produces a quasi-impulsive effect associated with the negative force trough.

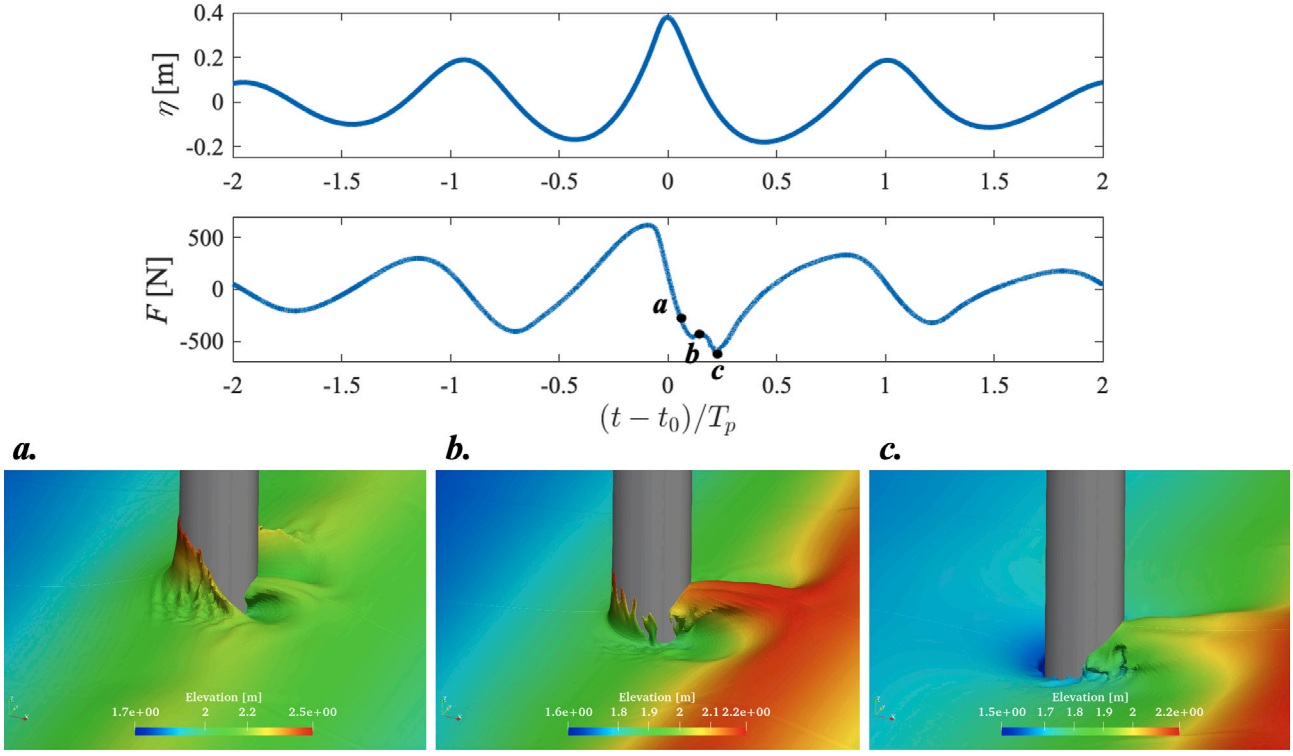

Fig. 4. Time histories of surface elevation η and force F, with three time points marked (top two panels). Bottom surface plots showing wave fields around the cylinder at the three times for CFD-02. Wave propagation is from left to right.

4. Data analysis

4.1. Harmonic separation and frequency limits

The four repeated runs with controlled initial phase shifts ϵ_0, at 90° increments, enable us to separate the harmonic contents of the simulated wave elevation, force, and moment signals. This so-called four-phase method (Fitzgerald et al., 2014) permits the isolation of principal harmonic contributions through simple linear combinations of the signals, supplemented by frequency filtering. Following the approach in Hlophe et al. (2025a), the nth harmonic is extracted by filtering over a frequency band $\boldsymbol{\Omega}_n$ centred around nf_p, where $f_p = 1/T_p$ is the spectral peak frequency. The lower and upper frequency limits, Ω_n^0 and Ω_n^∞, are defined from the spectrum $S_n(f)$ as $\boldsymbol{\Omega}_n = \left[\Omega_n^0, \Omega_n^\infty\right]$, where Ω_n^0 is the lowest frequency on the left-hand side of the spectral peak for which

$$S_n(f) \geq \frac{1}{1000} \max_f S_n(f),$$

and Ω_n^∞ is the highest frequency on the right-hand side satisfying the same criterion. This definition ensures that only energetically significant contributions to the nth harmonic are retained. Here, the spectrum $S_n(f)$ is generated from n powers of linear load, initially band-pass filtered over $\boldsymbol{\Omega}_1^\star = [0.6, 3]f_p$ based on linear theory; this interval is refined later. See further details in Hlophe et al. (2025a).

In this work, all signals are low-pass filtered at the upper frequency limit of the ninth harmonic, Ω_9^∞, to suppress noise contamination. Fig. 5 shows the simulated time histories of η, F, and M for the four input phases ϵ_0, for case CFD-02. This case, together with CFD-04 later, is selected because of its relatively high but realistic steepness, which reduces noise amplification in the higher bound harmonics. Nonlinearity becomes more pronounced moving down from η to M. A high-frequency wiggle appears on the down-crossing side of the trough in both F and M, associated with the so-called secondary load cycle (see, e.g. Grue et al., 1993; Riise et al., 2018; Hlophe et al., 2025b). The approximate 90° phase shift between η and F or η and M reaffirms that the loading is inertia-dominated.

The moment signals $M(t)$ exhibit stronger nonlinear features than the corresponding force $F(t)$, consistent with $M(t) = \sum M_n(t) = \sum L_n(t)F_n(t)$ where the effective lever arms $L_n(t)$ generally increase with harmonic number. The amplified M nonlinearity reflects both the intrinsic nonlinearity of η and the nonlinear wave–structure interaction, along with higher bound harmonics acting at longer arms along the cylinder, as discussed in Section 2.

Fig. 6 compares the extracted force harmonics F_n (left axis) and the corresponding moment harmonics M_n (right axis) for $n = 0$–9, highlighting their relative magnitudes. The $n = 0$ component corresponds to the slowly varying (difference-frequency) load, while $n \geq 1$ represent the oscillatory harmonics. The dominant nonlinear contribution occurs at the second-order sum-frequency (2+, $n = 2$), after which the harmonic amplitudes decrease progressively, at least up to $n = 5$, consistent with the expected decay of higher-order terms in a Stokes-type expansion. The second-order difference-frequency component (2−, $n = 0$) exhibits greater variability and appears less robustly extracted than the oscillatory harmonics, and differs somewhat from the behaviour observed in experimental force data reported by Hlophe et al. (2025a). This component may be more sensitive to very-low-frequency effects in finite numerical domains, whereas the higher harmonics are much less affected due to their relatively short length scales.

While minor phase and amplitude misalignments between F_n and M_n are visible, the third harmonic shows markedly poorer collapse than the others. That is, at 3+, $L_3(t) = M_3(t)/F_3(t)$ is not as close to constant in time as for all the other linear and sum components. This is attributed to the well-known distinctive behaviour of the third harmonic load previously reported in multiple experimental studies (e.g. Mj et al., 2023; Tang et al., 2024a) which is also consistent with the distinctive third-harmonic point-load contribution in the FNV framework. Hlophe et al. (2025a) noted that this anomalous behaviour also influences other harmonics that are multiples of $n = 3$.

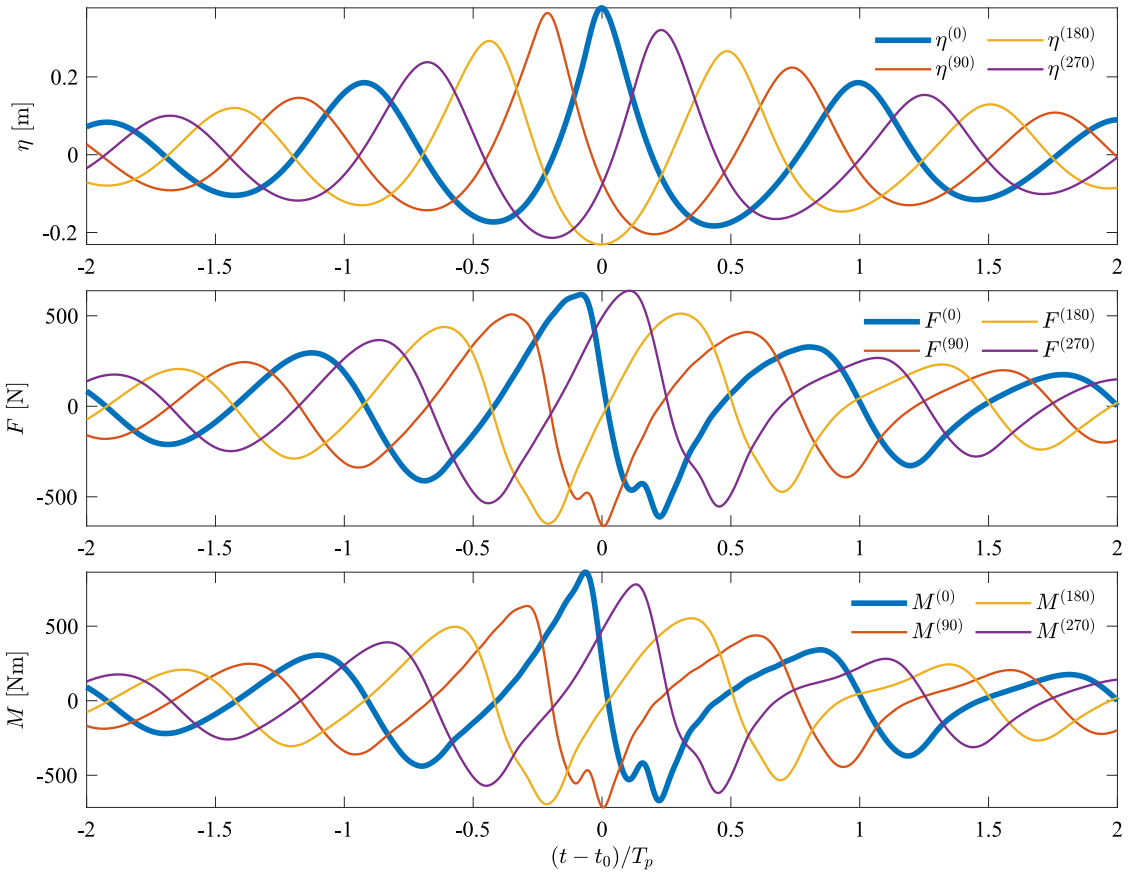

Fig. 5. Time histories of surface elevation η, force F, and moment M for the four phase-shifted runs, $\epsilon_0 = 0°, 90°, 180°, 270°$. The thicker line in each subplot corresponds to the CFD-02 run at $\epsilon_0 = 0°$, used as the reference case for subsequent harmonic separation.

4.2. Moment reconstruction from force

In the present testing regime, the loading is primarily inertia-dominated. In this case, the nonlinear convective acceleration terms, uu_x and wu_z, contribute comparatively little because they tend to offset one another. Fig. 2 of Taylor et al. (2024) shows that the depth integrals of these two terms result in similar force profiles of opposite signs, so that their combined effect is much smaller than either term taken individually. Motivated by this observation, we proceed under the simplifying assumption of inertia dominance, whereby the moments can be reconstructed directly by multiplying the extracted force harmonics by the corresponding moment arms.

4.2.1. Data-derived moment arms

The effective moment arm L_n for the nth harmonic is estimated directly from the CFD data (see Table 1) by examining whether the moment M_n and force F_n harmonics share the same temporal shape. If M_n and F_n are proportional in time, their ratio becomes time-invariant, yielding a constant moment arm for that harmonic. Demonstrating a constant-in-time moment arm for each harmonic would be both physically informative and practically useful. The following analysis tests whether this approximation holds for the present CFD cases. To do this, we plot $F_n(t)$ against $M_n(t)$ as parametric curves of F_n versus M_n, with time t as an implicit parameter. For each of the four input phase shifts ϵ_0, we determine the slope of the F_n–M_n relation and then average across all phases to obtain a robust estimate of the effective arm, denoted $\overline{L}_n$. On a linear wave basis, depth integrals of the velocity fields to the still-water level suggest this time invariance should hold, but our analysis examines harmonics up to approximately $n = 9$, where such a simplification becomes less certain.

To quantify how closely the force and moment harmonics collapse onto a linear relation, we also compute the squared Pearson correlation coefficient between F_n and M_n,

$$r_n^2(F_n, M_n) = \frac{\left(\langle F_n M_n\rangle - \langle F_n\rangle\langle M_n\rangle\right)^2}{\left(\langle F_n^2\rangle - \langle F_n\rangle^2\right)\left(\langle M_n^2\rangle - \langle M_n\rangle^2\right)}, \tag{4.1}$$

where $\langle\cdot\rangle$ denotes the time average over the analysis window. Values of r_n^2 close to unity indicate that $F_n(t)$ and $M_n(t)$ share nearly identical temporal structure and therefore support the assumption of a constant moment arm for that harmonic.

Fig. 7 illustrates the harmonic-based parametric curves of F_n and M_n. The inferred slopes are evaluated over the interval $-1.5 \le (t - t_0)/T_p \le 1.5$ to exclude the noisy ends of the records. The figure panels also annotate the resulting harmonic moment arms together with the regression coefficient $r^2_{FM,n}$ (Eq. (4.1)), averaged over the four input phases, for the representative cases CFD-02 and CFD-04.

Contrary to the monotonic increase predicted by theory, the data reveal more complex behaviour. Although the discrepancies are modest and the values remain broadly consistent with the theoretical predictions shown in Fig. 1, several deviations are apparent. Excluding $n = 0$, the ellipses associated with $n = 3$ and $n = 6$ appear visibly 'fatter' in both cases, indicating a weaker collapse onto a single linear relation between F_n and M_n. A plausible explanation is the distinctive FNV point load, which is predicted to arise at third order in wave amplitude and therefore appears as a third-frequency harmonic. The sixth harmonic may then be interpreted as a double-frequency contribution associated with this third-harmonic forcing. By contrast, the remaining even harmonics (apart from $n = 6$) appear noticeably 'slimmer' than their odd counterparts, indicating a closer collapse to a constant moment arm for each harmonic.

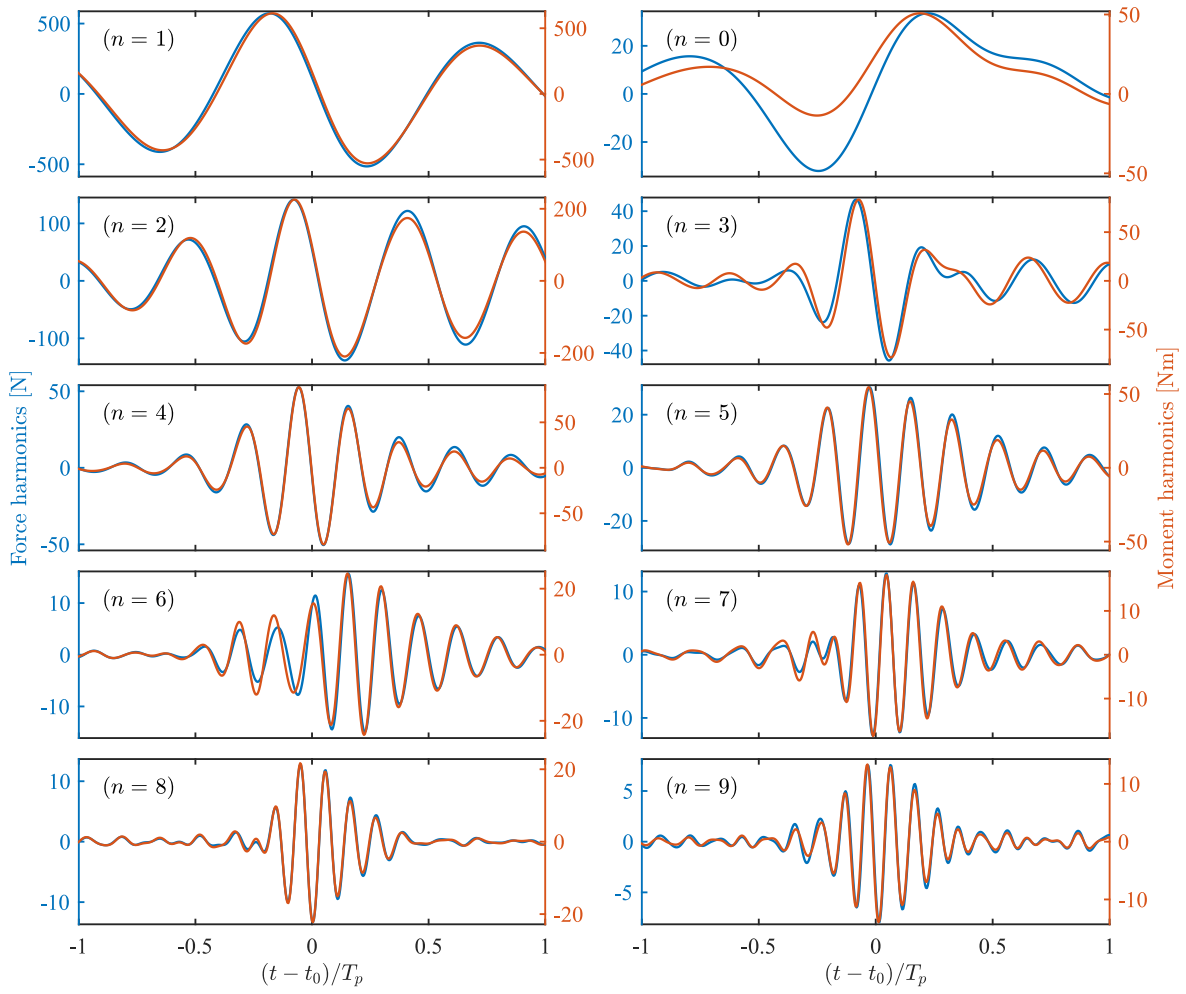

Fig. 6. Force F_n (blue line; left axis) and moment M_n (red line; right axis) harmonic components for representative modes n, obtained from the phase-decomposed signals of the $\epsilon_0 = 0°$ reference run shown in Fig. 5. Each panel shows the harmonic time histories with vertical scaling adjusted to emphasise the relative phasing.

For completeness, Fig. 8 compares the data-derived and theoretical moment arms ($z = 0$), averaged across all four phase runs. To characterise the central tendency of the measured moment arms, we computed an outlier-filtered mean for each harmonic. For a given set of moment arms $\{L_{n_i}\}_{i=1}^{N}$, statistical outliers were identified with MATLAB's 'isoutlier' function using the median absolute deviation (MAD) criterion and a threshold factor of 2. The filtered mean for the nth moment arm was then evaluated as

$$\overline{L_n} = \frac{1}{N^*} \sum_{i \in \mathcal{I}^*} L_{n_i},$$

where $\mathcal{I}^*$ is the index set of non-outlier samples and $N^* = |\mathcal{I}^*|$ its cardinality. These outlier-corrected means are shown in Fig. 8 as horizontal dashed lines. Additionally, theoretical means are plotted in a corresponding colour.

Fig. 8 shows several clear trends. The linear component ($n = 1$) shows virtually perfect agreement between CFD data and inertia-based theoretical predictions. No firm conclusion can be drawn for the sub-harmonic ($n = 0$) because the long-wave CFD runs are contaminated. However, the first four cases suggest $\overline{L}/h \approx 0.5$, consistent with expectations.

For the second harmonic ($n = 2$), the theoretical moment arms are consistently smaller than the CFD estimates by an approximately constant offset. A multiplicative factor of roughly 1.25 is required to reconcile the two, underscoring the strong contribution of the second harmonic to the total overturning moment. This scaling likely reflects the contribution associated with the movement of the free surface as $\eta_1 \partial L_1/\partial z$, evaluated at $z = 0$, which is a second harmonic term effectively acting close to the still-water level; second-order convective-acceleration terms omitted from the inertia-only kernel; or a small residual diffraction effect that does not perfectly cancel at the shorter length scale of 2+. The importance of the product term driving a second harmonic force close to the still-water level is demonstrated in Appendix. Such products of the free surface and local flow properties will be significant for all harmonics except the linear one.

For the third harmonic ($n = 3$), the CFD results indicate that the effective load application occurs closer to the free surface than predicted by the analytical expression, consistent with the free-surface-localised contribution identified in the FNV formulation and Rainey's theoretical framework (Kristiansen and Faltinsen, 2017). Although greater scatter is observed for this harmonic, the deviations are not systematic, suggesting no additional amplitude dependence beyond the assumed Stokes-type scaling. The corresponding constant scaling factor for $n = 3$ is approximately 1.3.

Harmonics $n = 4$ and $n = 5$ show close agreement with the theoretical prediction, with scaling factors of approximately 1.125, while higher-order harmonics display even better consistency but contribute little to design loads (Hlophe et al., 2025a).

While numerical artefacts in free-surface CFD can, in general, lead to local overprediction of velocities, the absence of any systematic dependence of the inferred moment-arm scaling on KC or numerical parameters suggests that such effects are not the primary cause of the discrepancies observed here.

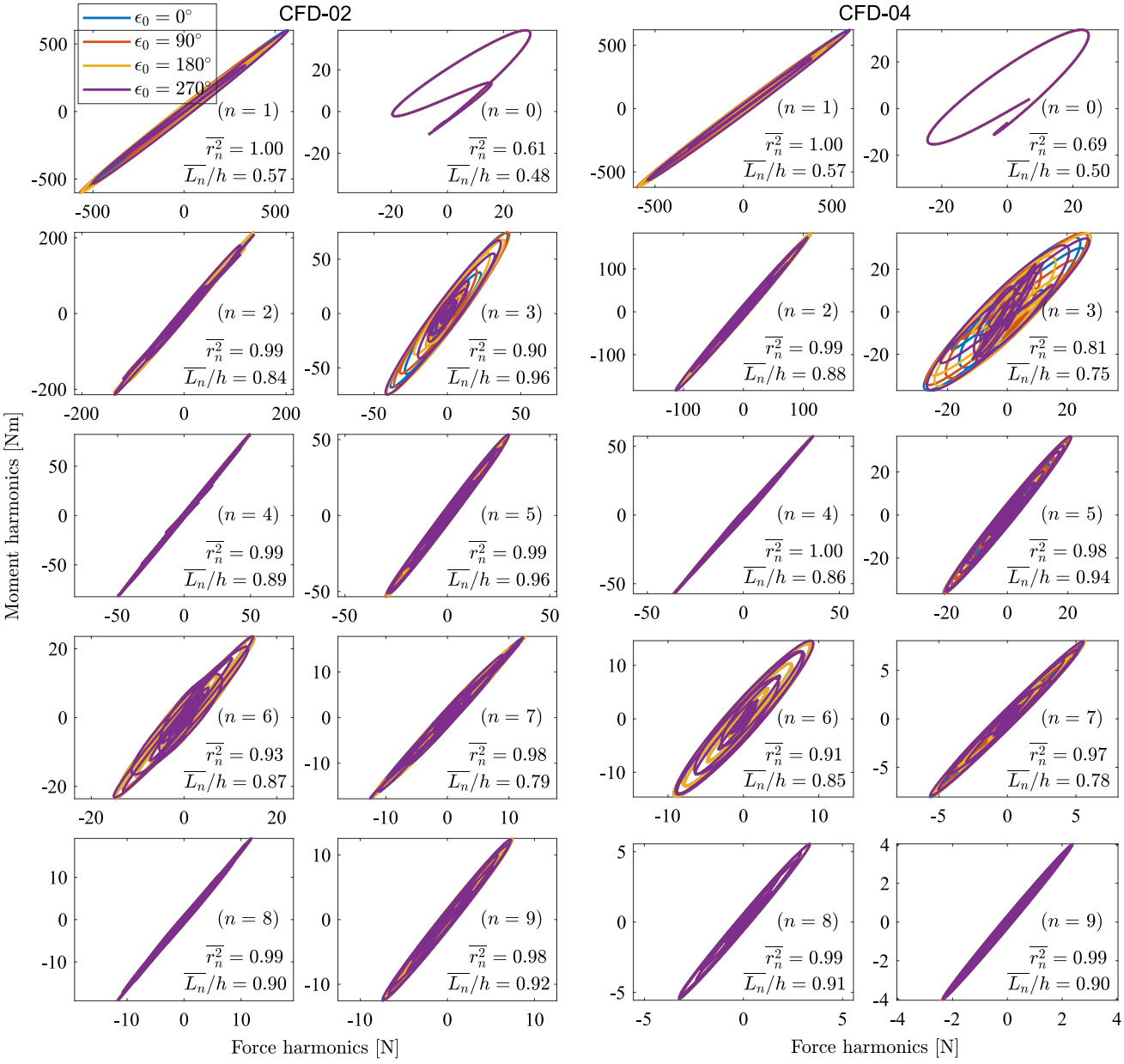

Fig. 7. Parametric plots of harmonic force F_n versus harmonic moment M_n for cases CFD-02 and CFD-04. The effective moment arms $\overline{L_n}$ are obtained as the slopes of the F_n–M_n relations and averaged over the four input phases. The regression coefficient $\overline{r_n^2}$ (Eq. (4.1)) is also reported in each panel as a measure of the linear collapse.

4.2.2. Harmonic reconstruction errors and interpretation

The comparison between theoretical and CFD-derived moment arms shows consistent offsets for the key harmonics. To account for these differences, we introduce harmonic-dependent scaling factors applied to the inertia-based theoretical moment arms. The scaling factors α_n are defined as the ratios of the means in the panels of Fig. 8:

$$\alpha_n = \begin{cases} 1.25, & n = 2, \\ 1.3, & n = 3, \\ 1.125, & n \in \{4, 5\}, \\ 1, & \text{otherwise}. \end{cases} \tag{4.2}$$

The scaled theoretical moment arms are therefore

$$L_n^{\text{scaled}} = \alpha_n \, L_n^{(u_t)},$$

leading to reconstructed moment harmonics

$$\widetilde{M}_n = L_n^{\text{scaled}} \, F_n.$$

The factors α_n represent corrections to the still-water inertia-based lever-arm kernel, rather than modifications to the F_n harmonics themselves. If F_n is obtained from another force model that already incorporates different free-surface or convective contributions, the same moment-arm framework may still be used; however, the optimal values of α_n may require recalibration for that model.

We next quantify the reconstruction accuracy associated with the two moment-arm formulations. Specifically, we test two reconstruction strategies:

(a) using still-water theoretical arms (depth integrals over $-h \le z \le 0$), and
(b) using data-derived arms obtained from parametric F_n–M_n plots.

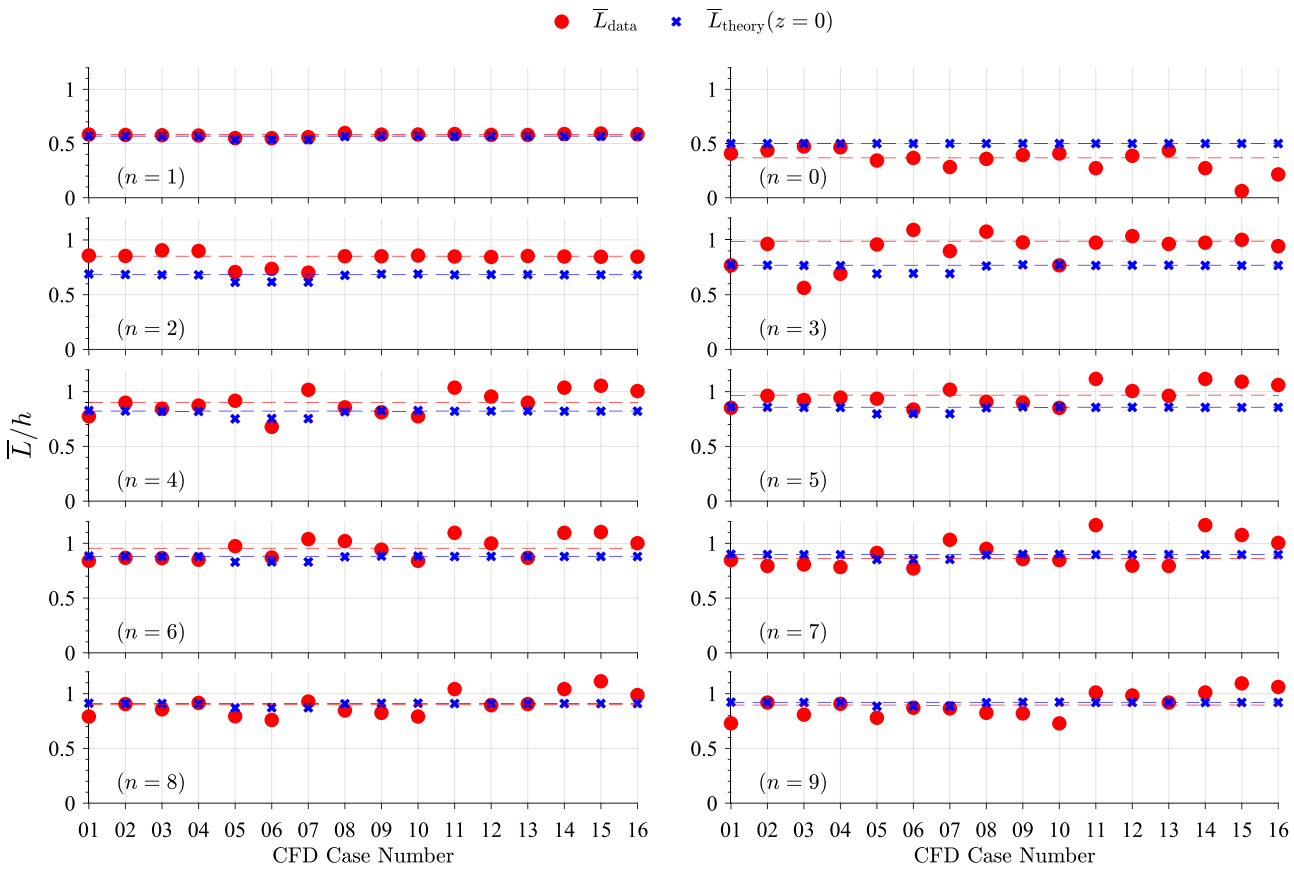

Fig. 8. Comparison of dimensionless moment arms $\overline{L_n}/h$ obtained from the data (red) and from inertia-based theoretical predictions evaluated over $-h \le z \le 0$ (blue). For each harmonic, the horizontal dashed lines indicate the outlier-filtered mean across all CFD cases (median rule with threshold factor 2).

Based on the previous scaling issue, we apply the constant α_n (4.2) scale factors to the $2 \le n \le 5$ theoretical arms.

To quantify the accuracy of the reconstructed moment harmonics, we adopt the same error measure used previously for force reconstruction (Hlophe et al., 2025b). Specifically, for each harmonic number n, the time-averaged, normalised mean-squared error is defined as

$$\langle \mathcal{E}_n(t) \rangle = \frac{1}{2T_p} \int_{-T_p}^{T_p} \frac{\left| M_n(t) - \widetilde{M}_n(t) \right|^2}{\widehat{M}_n^2/4} \, \mathrm{d}t, \tag{4.3}$$

where $M_n(t)$ is the simulated nth-order moment, $\widetilde{M}_n(t)$ is the corresponding reconstruction, and $\widehat{M}_n$ denotes the envelope amplitude of the simulated harmonic. The averaging interval $[-T_p, T_p]$ is chosen to encompass the wave group as well as regions exhibiting the secondary load cycle while avoiding portions in the tails dominated by noise. Errors are further averaged over the four phase-shifted runs to obtain a consistent case-level measure.

The theoretical moment arms for the inertia term u_t follow from the depth-integral kernels derived in Section 2. These kernels depend on the effective wavenumber $\hat{k}$, which is evaluated as described in Section 2 using the zero-crossing period $T_{m02} = \sqrt{m_0/m_2}$ of the first-harmonic free-surface elevation.

$$m_n = \int_0^\infty f^n \, S_{\eta\eta}(f) \, \mathrm{d}f,$$

where $S_{\eta\eta}(f)$ is the power spectral density of $\eta(t)$. To compute the power spectrum, we use $\eta \to \eta_1$, noting that within linear theory $T_{m02}(\eta_1) \approx T_{m02}(F_1)$.

Fig. 9 presents the time-averaged, normalised mean-squared errors $\langle \mathcal{E}_n \rangle$ (4.3) for all CFD cases. A consistent trend emerges: the theoretical arms L_{theory} (with scaling) perform nearly as well as the data-derived arms (assumed to represent the target) across most conditions. Where differences do occur, the associated errors remain small, generally below 0.1. For $n \in \{0, 1\}$, the theoretical and data-derived results match exactly, since no lower-order potential terms exist. In the nonlinear terms, minor discrepancies between the theoretical and data-derived arms likely arise from phase differences between the lower-order potential components and the measured (or 'target') M_n/F_n relationships. Nevertheless, the error analysis confirms that constant, inertia-based moment arms evaluated at $z = 0$, when appropriately scaled for each harmonic, provide a robust and computationally efficient reconstruction of the overturning moment in the present testing regime. Within the present range of wave conditions, no systematic dependence of the reconstructed moment errors on KC is observed, indicating that inertia remains the dominant contributor to the overturning moment even for cases with $KC \gtrsim 7.5$.

4.2.3. Moment time-series reconstruction

Utilising the pair of moment arms established, L_{data} and L_{theory}, we next compare the reconstructed and simulated moment time histories. Fig. 10 illustrates the individual harmonic reconstructions for case CFD-02. For all $n \ge 1$, the agreement is clear, though small amplitude offsets remain because the applied scaling is based on an average factor. These minor discrepancies have little influence on the total moment, as shown in Fig. 11, which presents the full reconstructed signal for five representative cases. Each reconstruction reproduces the dominant loading cycle well, and the data-derived moment arms offer only a slight improvement over the scaled still-water theory in the trough that contains the secondary load cycle. For practical purposes, this secondary load is negligible for adequately damped structures, as demonstrated by Hlophe et al. (2025a).

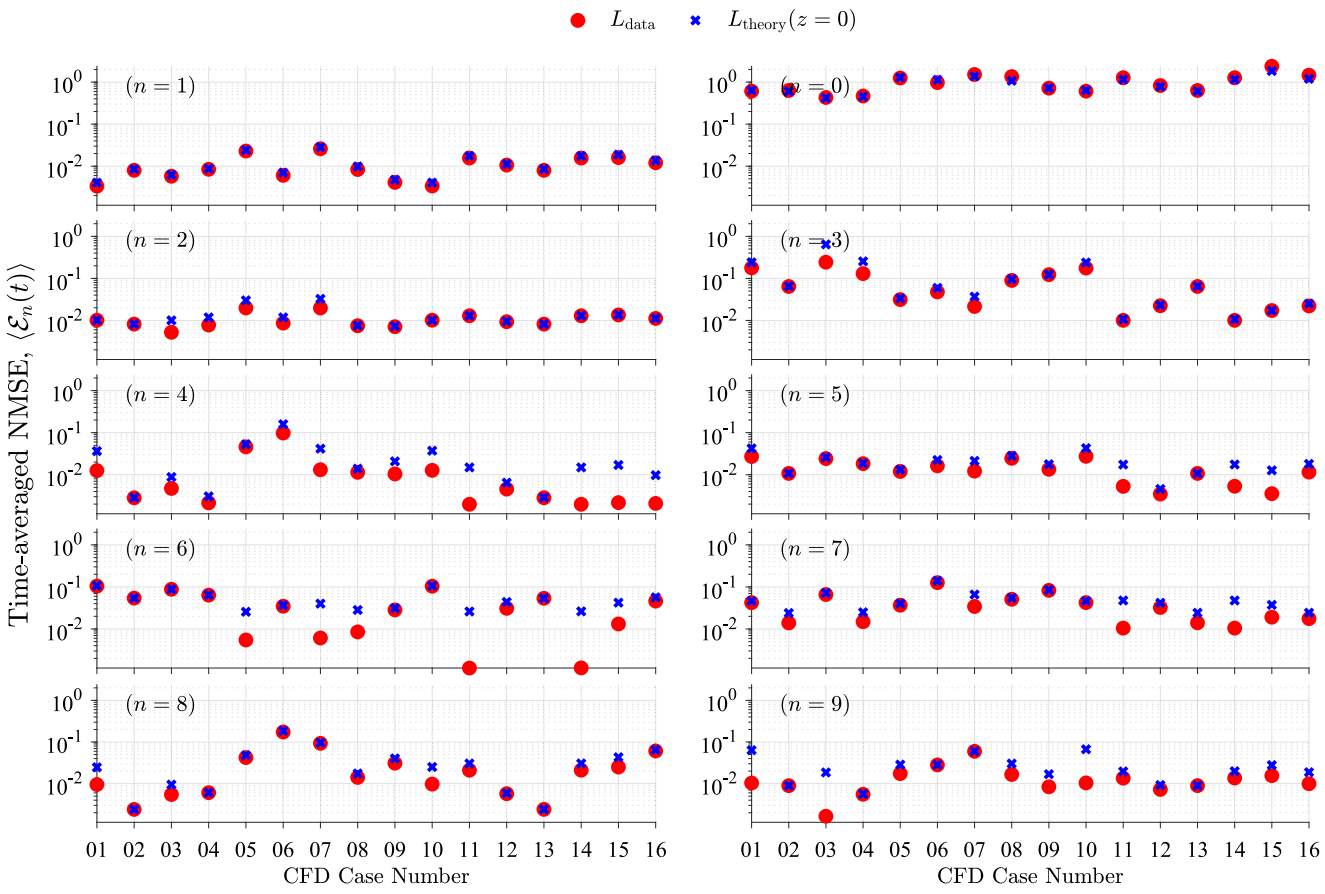

Fig. 9. Time-averaged error $\langle \mathcal{E}_n(t) \rangle$ for the reconstruction of moment harmonics across all cases. Comparison is made between reconstructions using two moment-arm definitions: data-derived L_{data} and theoretical L_{theory} moment arms.

4.3. Implications for monopile foundation design

This study clarifies how higher-order wave harmonics influence the effective moment arm of wave-induced overturning moments on a vertical cylinder. For engineering design, the central outcome is that the inertia term alone provides a dependable baseline for estimating the moment arm across the tested conditions, which are representative of inertia-dominated monopile loading. Reconstructions using still-water theoretical arms reproduce the dominant overturning-moment cycle and preserve the observed harmonic content with high fidelity.

The analysis also identifies a systematic scaling requirement for the second through fifth superharmonics, with the third harmonic behaving as an exception, as it acts predominantly at the free surface. This scaling is straightforward to apply in practice.

From a design standpoint, these findings show that simplified inertia-only assumptions, augmented with the harmonic-specific scaling, remain appropriate for estimating overturning moments on monopile foundations. The upward shift of the effective load application point for the third harmonic further underscores the importance of free-surface effects when assessing extreme events or fatigue loading in shallow water. Incorporating these refined lever arms into standard design calculations reduces the risk of underestimating bending moments in severe sea states. Within the present dataset, no significant dependence on wave steepness or cylinder diameter is observed, in contrast to the trends reported by Feng et al. (2020).

5. Conclusion

This study has presented a harmonic-based framework for analysing nonlinear wave-induced overturning moments on cylindrical monopile foundations using depth-integrated acceleration terms from the Morison formulation. The aim was to isolate the effective moment arms associated with individual harmonic components of the hydrodynamic force, which are central to the design of fixed offshore wind turbines operating in inertia-dominated conditions. CFD simulations were used to validate the harmonic-by-harmonic reconstruction of the overturning moment $\widetilde{M}(t)$ from the simulated hydrodynamic force $F(t)$ using constant-in-time moment arms.

Two reconstruction strategies were examined:

(a) theoretical arms obtained from depth integrations up to the still-water level, $z = 0$;
(a) data-derived arms estimated from the slope of harmonic force–moment regressions.

The zeroth harmonic is excluded from the conclusions because of residual low-frequency distortion in the CFD results.

The main findings are as follows:

(a) Harmonic components of the overturning moment M_n are directly proportional to the corresponding harmonic force F_n, connected through a constant length scale that remains nearly invariant in time as wave groups pass the cylinder. This proportionality defines an effective moment arm that is both simple to extract and physically meaningful.
(a) The moment arm derived from the Morison inertia term provides a reliable baseline estimate for the harmonics relevant to the present monopile applications, allowing convective accelerations to be neglected with little loss of accuracy in the present inertia-dominated regime.

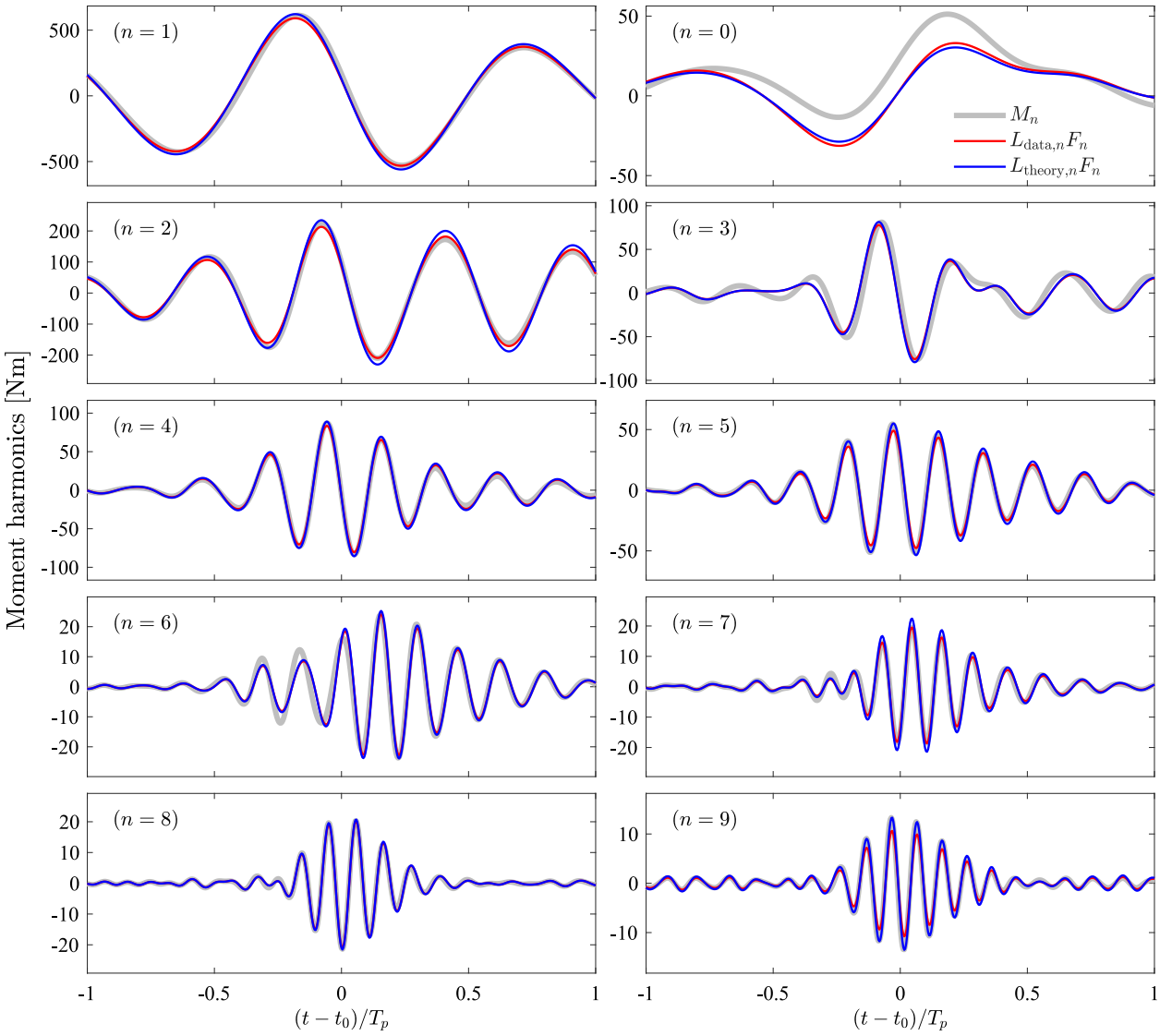

Fig. 10. Comparison of CFD-derived harmonic overturning moment time histories (M_n, thick grey line) with reconstructions based on (a) data-derived moment arms, $L_{\mathrm{data},n}F_n$, and (b) scaled still-water moment arms, $L_{\mathrm{theory},n}F_n$. Results are shown for case CFD-02 with initial phase $\epsilon_0 = 0°$.

(b) The effective moment arms remain nearly constant across harmonics in different testing conditions, with modest corrections only for the nonlinear components. The second harmonic typically requires a correction of order 25%, while the third harmonic is centred near the still-water level, consistent with theoretical point-load expectations, and requires a 30% correction. The fourth and fifth harmonics require corrections of order 12.5%, while higher orders need no significant adjustment. These corrections emphasise the importance of loading components acting close to the free surface, arising from surface displacement and products involving lower-harmonic flow components.

These results demonstrate that moment and force harmonics share a simple, time-invariant proportionality, allowing nonlinear overturning moments to be reconstructed directly once the harmonic force components are known. This approach provides a practical framework for generalising to a broad range of sea states, including those in the SeaSwallows database.

When combined with the well-established higher-order Stokes models used for force prediction (see, e.g. Chen et al., 2018; Feng et al., 2020; Hlophe et al., 2025a), the present method offers an efficient hybrid moment formulation:

$$M_n(t) \approx L_n^{\mathrm{scaled}} F_n(t),$$

where L_n^{scaled} are the inertia-based, constant moment arms, appropriately scaled with simple factors in Eq. (4.2). The scaling factors α_n therefore represent corrections to the still-water inertia-based lever-arm kernel rather than to the force model itself. When the harmonic forces F_n are obtained from alternative force models used in design analyses, the same moment-arm framework may still be applied; however, the optimal values of α_n may require recalibration. Nevertheless, the present results suggest that the overall trend of nearly constant moment arms across harmonics and cases should remain robust for inertia-dominated wave–structure interactions.

In summary, the analysis shows that inertia-driven moment-arm estimation, combined with simple harmonic corrections, provides a physically transparent and computationally efficient framework for incorporating nonlinear overturning moments in monopile designs. Although future laboratory studies with improved resolution of subharmonic components would help refine the results, the present analysis

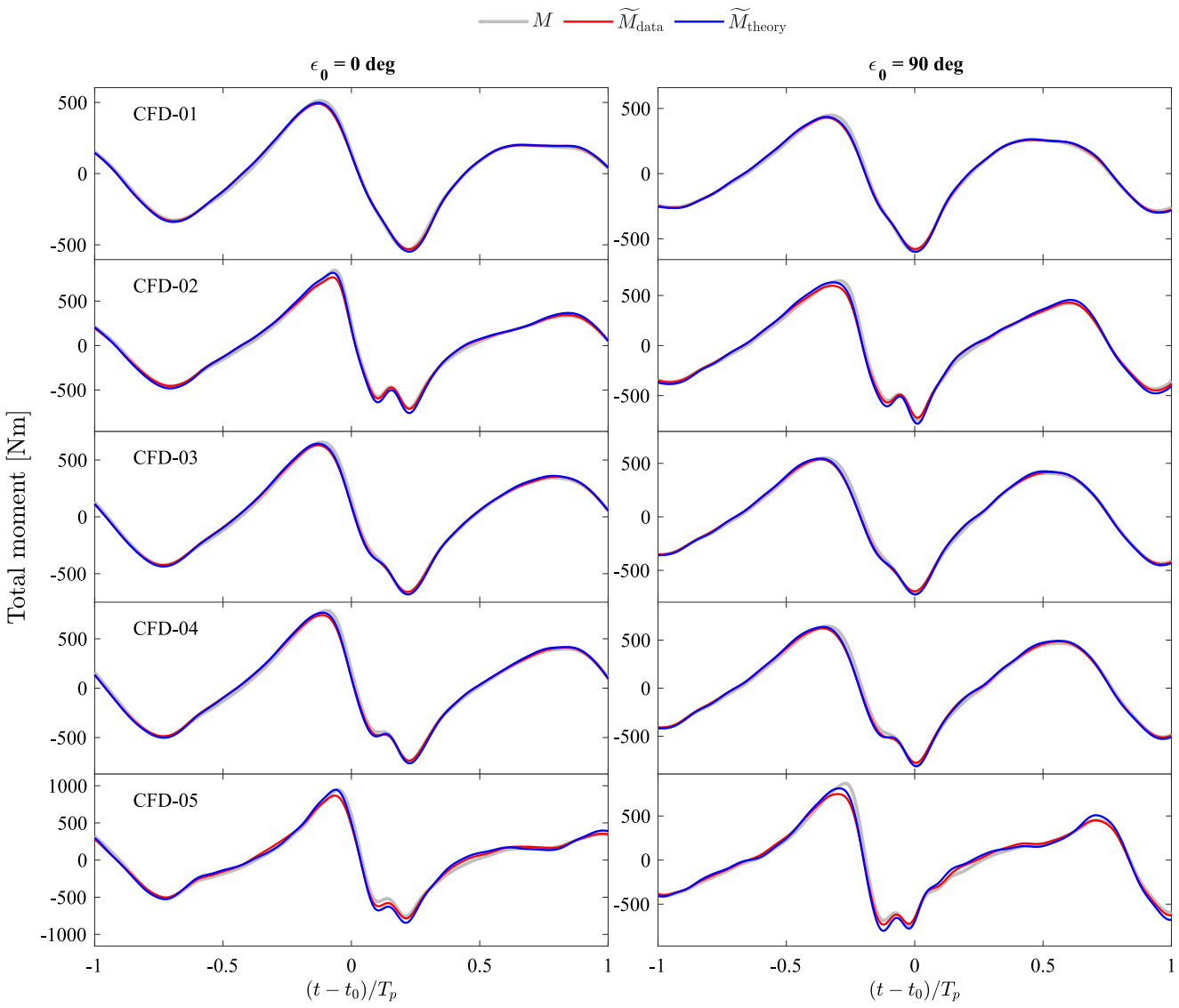

Fig. 11. Comparison of the total CFD-derived overturning moment time history (M, thick grey line) with reconstructions obtained by summing harmonic contributions using (a) data-derived moment arms, $\widetilde{M}_{\text{data}} = \sum_n L_{\text{data},n} F_n$, and (b) still-water moment arms, $\widetilde{M}_{\text{theory}} = \sum_n L_{\text{theory},n} F_n$. Results are shown for cases CFD-01–05 and initial phases $\epsilon_0 = 0°$ and 90°, corresponding to the largest observed secondary load cycle where present.

already offers a practical approach for representing nonlinear moment contributions in offshore wind applications.

CRediT authorship contribution statement

Thobani Hlophe: Writing – review & editing, Writing – original draft, Visualization, Software, Methodology, Formal analysis, Conceptualization. **Thomas A.A. Adcock:** Writing – review & editing, Supervision, Resources, Funding acquisition. **Haoyu Ding:** Writing – review & editing, Visualization, Software, Data curation. **Jun Zang:** Writing – review & editing, Resources, Funding acquisition. **Paul H. Taylor:** Writing – review & editing, Supervision, Methodology, Conceptualization.

Declaration of competing interest

The authors declare that they have no known competing financial interests or personal relationships that could have appeared to influence the work reported in this paper.

Acknowledgements

This research is funded by EPSRC grant EP/V050079/1. Simulations are supported by EPSRC grant EP/X035751/1.

Appendix. Origin of the upward shift in the second-order moment arm

This appendix provides a concise derivation of the mechanism described in the main text that causes the effective moment arm of the second harmonic to be shifted upward relative to that obtained by integrating the inertia term up to still-water level ($z = 0$). The argument follows from two contributions to the 2ω ('2+') load:

1. a direct second-order potential contribution at frequency 2ω;
2. a geometric contribution arising from integrating the first-order acceleration u_t from $z = 0$ up to the instantaneous free surface η_1, which produces a second harmonic through the product $\frac{\partial u_1}{\partial t}|_{z=0}\,\eta_1$.

For clarity, the derivation below omits the common inertia coefficient $2\rho\pi R^2$ in the formulation, as the focus here is on the vertical distribution and scaling of the acceleration term u_t.

Both contributions scale as a^2, share the same second-harmonic frequency and phase, but differ in their vertical distribution. The surface contribution acts near the free surface and therefore produces a larger moment per unit force than the subsurface potential contribution. The derivation below sketches these two terms and shows how their sum leads to an upward shift in the effective moment arm.

Linear (first-order) fields

For a monochromatic linear wave, the first-order free-surface elevation and horizontal velocity are

$$\eta_1(t) = a\cos\omega t, \qquad u_1(z,t) = a\omega\frac{\cosh[k(h+z)]}{\sinh kh}\cos\omega t,$$

and the local acceleration is

$$\frac{\partial u_1}{\partial t} \equiv \dot{u}_1(z,t) = -a\omega^2\frac{\cosh[k(h+z)]}{\sinh kh}\sin\omega t.$$

(1) Direct second-order potential contribution

The second-order potential generates a 2ω horizontal velocity component with vertical structure proportional to $\cosh[2k(h+z)]/\sinh(2kh)$. The 2ω part of the acceleration is therefore

$$\dot{u}_2^{(\mathrm{pot})}(z,t) \approx C_2^{\mathrm{pot}}\frac{\cosh[2k(h+z)]}{\sinh 2kh}\sin 2\omega t, \qquad C_2^{\mathrm{pot}} \sim \omega^2 a(ak),$$

where ka is the wave steepness. The force amplitude (per unit horizontal length) from this term is

$$F_2^{(\mathrm{pot})} \propto C_2^{\mathrm{pot}}\int_{-h}^{0}\frac{\cosh[2k(h+z)]}{\sinh 2kh}\,\mathrm{d}z = \frac{C_2^{\mathrm{pot}}}{2k}.$$

The corresponding moment integral,

$$M_2^{(\mathrm{pot})} \propto C_2^{\mathrm{pot}}\int_{-h}^{0}(z+h)\frac{\cosh[2k(h+z)]}{\sinh 2kh}\,\mathrm{d}z,$$

yields an effective moment arm

$$L_2^{(\mathrm{pot})} = \frac{M_2^{(\mathrm{pot})}}{F_2^{(\mathrm{pot})}} = h\,\mathcal{F}_{\mathrm{pot}},$$

where $0.5 \le \mathcal{F}_{\mathrm{pot}}(kh) \le 1$ is a known bounded function that increases with increasing kh as shown by the yellow curve for $n = 2$ in Fig. 1.

(2) Surface (geometric) contribution

Integrating the first-order acceleration $\dot{u}_1$ from $z = 0$ up to the instantaneous free surface gives

$$F^{(\mathrm{surf})}(t) \propto \dot{u}_1(z=0,t)\,\eta_1(t).$$

Using $\dot{u}_1(z=0,t)$ and $\eta_1(t)$, we obtain

$$F^{(\mathrm{surf})}(t) \propto -\frac{1}{2}a^2\omega^2\frac{\cosh kh}{\sinh kh}\sin 2\omega t.$$

This 2ω component has the same phase as the potential term and acts effectively at the free surface, so its associated moment is

$$M^{(\mathrm{surf})}(t) \approx h\,F^{(\mathrm{surf})}(t).$$

(3) Total 2ω load and effective moment arm

The total second-harmonic force and moment are

$$F_2 = F_2^{(\mathrm{pot})} + F^{(\mathrm{surf})}, \qquad M_2 = M_2^{(\mathrm{pot})} + M^{(\mathrm{surf})}.$$

The combined effective moment arm is

$$L_2 = \frac{M_2}{F_2} = \frac{M_2^{(\mathrm{pot})} + h\,F^{(\mathrm{surf})}}{F_2^{(\mathrm{pot})} + F^{(\mathrm{surf})}} = h\frac{F_2^{(\mathrm{pot})}\mathcal{F}_{\mathrm{pot}} + F^{(\mathrm{surf})}}{F_2^{(\mathrm{pot})} + F^{(\mathrm{surf})}} \ge h\,\mathcal{F}_{\mathrm{pot}}.$$

If $F^{(\mathrm{surf})}$ is non-negligible, L_2 is biased towards the larger lever arm, i.e. $L_2 \to h$. Since both terms scale with a^2, this shift is independent of wave amplitude and depends only on kh.

Remarks and extension

- The same reasoning extends to higher bound harmonics: each receives contributions from direct higher-order potentials and geometric products such as $\eta_i\dot{u}_j$, which act near the surface and bias the moment arm upward.
- In deep water, the potential contribution decays with depth, increasing the relative weight of the surface term and enhancing the upward shift.
- Convective terms (uu_x, wu_z) also contribute at higher order. They often partially cancel but can still influence the balance between $F^{(\mathrm{pot})}$ and $F^{(\mathrm{surf})}$, thus modifying L_n.

This two-term decomposition — direct higher-order potential plus geometric (surface) correction — explains why the second harmonic, and sometimes higher bound harmonics, exhibit larger effective moment arms than predicted by the still-water integration of the inertia term. The shift depends primarily on kh and not on wave amplitude.

Data availability

Data will be made available on request.

References

Chen, L., Zang, J., Hillis, A., Morgan, G., Plummer, A., 2014. Numerical investigation of wave–structure interaction using OpenFOAM. Ocean Eng. 88, 91–109. http://dx.doi.org/10.1016/j.oceaneng.2014.06.003.

Chen, L.F., Zang, J., Taylor, P.H., Sun, L., Morgan, G.C.J., Grice, J., Orszaghova, J., Ruiz, M.T., 2018. An experimental decomposition of nonlinear forces on a surface-piercing column: Stokes-type expansions of the force harmonics. J. Fluid Mech. 848, 42–77.

Ding, H., Tang, T., Taylor, P.H., Adcock, T., Zhao, G., Dai, S., Hlophe, T., Reale, C., Zang, J., 2025. An investigation of the secondary load cycle associated with wave scattering in severe wave–cylinder interactions. J. Fluid Mech. 1021, A24. http://dx.doi.org/10.1017/jfm.2025.10738.

Faltinsen, O.M., Newman, J.N., Vinje, T., 1995. Nonlinear wave loads on a slender vertical cylinder. J. Fluid Mech. 289, 179–198.

Feng, X., Taylor, P.H., Dai, S., Day, A.H., Willden, R.H.J., Adcock, T.A.A., 2020. Experimental investigation of higher harmonic wave loads and moments on a vertical cylinder by a phase-manipulation method. Coast. Eng. 160, 103747.

Fitzgerald, C.J., Taylor, P.H., Eatock Taylor, R., Grice, J., Zang, J., 2014. Phase manipulation and the harmonic components of ringing forces on a surface-piercing column. Proc. R. Soc. A: Math. Phys. Eng. Sci. 470 (2168), 20130847.

Grue, J., Bjørshol, G., Strand, Ø., 1993. Higher harmonic wave exciting forces on a vertical cylinder. Prepr. Ser. Mech. Appl. Math..

Hlophe, T., Adcock, T.A.A., Ding, H., Zang, J., Dai, S., Tang, T., Taylor, P.H., 2025a. Nonlinear wave loads on monopile foundations and structural response in severe wave conditions. Appl. Ocean Res. 164, 104790.

Hlophe, T., Taylor, P.H., Ding, H., Zang, J., Dai, S., Adcock, T.A.A., 2025b. Resolving the secondary load cycle on vertical cylinders using high-order Stokes expansions. (Under review).

Horn, J.-T.H., Krokstad, J.R., Amdahl, J., 2016. Hydro-elastic contributions to fatigue damage on a large monopile. Energy Procedia 94, 102–114.

Jacobsen, N., Fuhrman, D., Fredsøe, J., 2012. A wave generation toolbox for the open-source CFD library: OpenFoam®. Internat. J. Numer. Methods Fluids 70 (9), 1073–1088.

Kristiansen, T., Faltinsen, O.M., 2017. Higher harmonic wave loads on a vertical cylinder in finite water depth. J. Fluid Mech. 833, 773–805.
Larsen, B.E., Fuhrman, D.R., Roenby, J., 2019. Performance of interfoam on the simulation of progressive waves. Coast. Eng. J. 61 (3), 380–400.
Li, Y., Fuhrman, D.R., 2022. On the turbulence modelling of waves breaking on a vertical pile. J. Fluid Mech. 953, A3.
Manners, W., Rainey, R., 1992. Hydrodynamic forces on fixed submerged cylinders. Proc. R. Soc. Lond. Ser. A: Math. Phys. Sci. 436 (1896), 13–32.
Mj, D., McAllister, M.L., Bredmose, H., Adcock, T.A.A., Taylor, P.H., 2023. Harmonic structure of wave loads on a surface piercing column in directionally spread and unidirectional random seas. J. Ocean. Eng. Mar. Energy 9 (3), 415–433.
Riise, B.H., Grue, J., Jensen, A., Johannessen, T.B., 2018. High frequency resonant response of a monopile in irregular deep water waves. J. Fluid Mech. 853, 564–586.
Ryan, G.V., Tang, T., McAdam, R.A., Adcock, T.A.A., 2025. Influence of non-linear wave load models on monopile supported offshore wind turbines for extreme conditions. Ocean Eng. 323, 120510.
Tang, T., Ding, H., Dai, S., Taylor, P.H., Zang, J., Adcock, T.A.A., 2024a. An experimental study of a quasi-impulsive backwards wave force associated with the secondary load cycle on a vertical cylinder. J. Fluid Mech. 994, A9.
Tang, T., Ryan, G., Ding, H., Chen, X., Zang, J., Taylor, P.H., Adcock, T.A.A., 2024b. A new Gaussian Process based model for non-linear wave loading on vertical cylinders. Coast. Eng. 188, 104427.
Taylor, P.H., Tang, T., Adcock, T.A.A., Zang, J., 2024. Transformed-FNV: Wave forces on a vertical cylinder—A free-surface formulation. Coast. Eng. 189, 104454.
Tromans, P.S., Anaturk, A.R., Hagemeijer, P., 1991. A new model for the kinematics of large ocean waves-application as a design wave. In: ISOPE International Ocean and Polar Engineering Conference. ISOPE, pp. ISOPE–I.